

DOT/FAA/TC-21/8

Federal Aviation Administration
William J. Hughes Technical Center
Aviation Research Division
Atlantic City International Airport
New Jersey 08405

A Study on Experimental Tests and Numerical Simulations of Boeing 747 Overhead Inaccessible-Area Fires

March 21, 2021

Final report



U.S. Department of Transportation
Federal Aviation Administration

NOTICE

This document is disseminated under the sponsorship of the U.S. Department of Transportation in the interest of information exchange. The U.S. Government assumes no liability for the contents or use thereof. The U.S. Government does not endorse products or manufacturers. Trade or manufacturers' names appear herein solely because they are considered essential to the objective of this report. The findings and conclusions in this report are those of the author(s) and do not necessarily represent the views of the funding agency. This document does not constitute FAA policy. Consult the FAA sponsoring organization listed on the Technical Documentation page as to its use.

This report is available at the Federal Aviation Administration William J. Hughes Technical Center's Full-Text Technical Reports page: actlibrary.tc.faa.gov in Adobe Acrobat portable document format (PDF).

Form DOT F 1700.7 (8-72)

Reproduction of completed page authorized

1. Report No. DOT/FAA/TC-21/8		2. Government Accession No.		3. Recipient's Catalog No.	
4. Title and Subtitle A Study on Experimental Tests and Numerical Simulations of Boeing 747 Overhead Inaccessible-Area Fires		5. Report Date March, 2021		6. Performing Organization Code ANG-E2	
		8. Performing Organization Report No.			
7. Author(s) Haiqing Guo ¹ , Marcos Vanella ² , Richard E. Lyon ³ , Randall McDermott ² , Sean Crowley ³ , Paul Scrofani ¹		9. Performing Organization Name and Address 1 Diakon Solutions LLC, 110 W Beaver Dr, Cape May Court House, NJ 08210 2 Fire Research Division, National Institute of Standards and Technology, Gaithersburg, MD 20899 3 Federal Aviation Administration, William J. Hughes Technical Center, Atlantic City Airport, NJ 08405		10. Work Unit No. (TRAIS)	
12. Sponsoring Agency Name and Address U.S. Department of Transportation FAA Northwest Mountain Regional Office 1601 Lind Avenue SW Renton, WA 98057		11. Contract or Grant No.		13. Type of Report and Period Covered Final Report	
		14. Sponsoring Agency Code AIR-600			
15. Supplementary Notes					
16. Abstract Hidden fire in an aircraft overhead inaccessible-area is hazardous to in-flight safety and could lead to catastrophic disaster. In this case, fire detection at the earliest stage requires an improved understanding of the heat and mass transfer in overhead areas with curved fuselage sections. In this effort, an experimental campaign was conducted at the FAA William J. Hughes Technical Center on different fire scenarios for the Boeing747-SP overhead inaccessible-area to advance knowledge on this phenomenon and provide validation data for the Fire Dynamics Simulator (FDS). Extensive work has been done recently to enable computer simulation of fire on complex geometries within this tool. Therefore, we use the experimental data obtained to perform validation of said capability. Model validation results are defined in terms of thermocouple readings measured and computed with satisfactory overall agreement.					
17. Key Words Fire modeling, aircraft fires, inaccessible-area fire experiment, heat transfer, fluid dynamics, CFD validation			18. Distribution Statement This document is available to the U.S. public through the National Technical Information Service (NTIS), Springfield, Virginia 22161. This document is also available from the Federal Aviation Administration William J. Hughes Technical Center at actlibrary.tc.faa.gov .		
19. Security Classif. (of this report) Unclassified		20. Security Classif. (of this page) Unclassified		21. No. of Pages 42	22. Price

Acknowledgements

We thank Dr. Emanuele Gissi of Corpo Nazionale dei Vigili del Fuoco (Italian Fire and Rescue Service), for converting in BlenderFDS the LIDAR generated model into FDS readable geometries. BlenderFDS is funded by a grant from the Italian Ministry of Foreign Affairs and International Cooperation.

Contents

1	Introduction	1
2	Experimental method	2
3	Numerical method	4
3.1	Cut-cell method for scalar transport and energy	4
3.2	Immersed boundary method on cut-cell region and wall model.....	8
4	Boeing 747 overhead inaccessible-area validation cases	10
4.1	Fire scenarios.....	10
4.2	Simulation setup.....	11
5	Results	13
5.1	Case 1 temperatures	15
5.2	Case 2 temperatures	19
5.3	Case 3 temperatures	22
5.4	Uncertainty analysis	26
6	Summary	28
7	References	30

Figures

Figure 1. Diagram of the full-scale test article: (a) Boeing B747-SP with highlighted overhead area, (b) LIDAR generated 3-D model	3
Figure 2. Detailed layout of burner, thermocouple, and thermocouple tree: (a) aerial view of the crown of fuselage, (b) side view of one representative thermocouple tree	4
Figure 3. Regular Cartesian and cut-cell grids: (a) Cut-cell region defined around triangulated spherical surface, (b) Cut-cells defined from C-shaped beam, and 2 refinement level interpretation	6
Figure 4. Cut-cell and faces in 2D: (a) Cut-cell ii surrounded by gas phase regular and cut-faces (3-6), and boundary cut-faces (1-2). (b) Interpolation sketch for wall modeled immersed boundary reconstruction of cut-face velocities	8
Figure 5. Front burner model setup: Overhead inaccessible-area surfaces in grey and burner defined in red. Roof and tree thermocouples are defined in green. Modeled region is divided in 144 FDS fluid meshes (black wireline) for fine grid cases.....	12
Figure 6. Example fire test photo and steady state temperature slice at $y = 3$ m for Case 1	14
Figure 7. Representative temperature slices at: (a) $y = 3$ m, (b) $x = 2.3$ m in Case 1. Time $t = 300$ s. Temperature units are in $^{\circ}\text{C}$	16
Figure 8. Measured (solid line) and modeled (dash line) temperature results of TCs at center along x direction (front – aft) in Case 1	16
Figure 9. Measured (solid line) and modeled (dash line) temperature results of TCs near front burner along y direction (side – side) in Case 1.....	17
Figure 10. Measured (solid line) and modeled (dash line) temperature results of TCs at TC Tree A in Case 1.....	18
Figure 11. Contour map of measured (solid line) and modeled (dash line) temperature results of crown TCs in Case 1.	18
Figure 12. Representative temperature slices at: (a) $y = 3$ m, (b) $x = 2.3$ m in Case 2. Time $t = 300$ s. Temperature units are in $^{\circ}\text{C}$	19
Figure 13. Measured (solid line) and modeled (dash line) temperature results of TCs at center along x direction (front – aft) in Case 2.....	20
Figure 14. Measured (solid line) and modeled (dash line) temperature results of TCs near front burner along y direction (side – side) in Case 2.....	20
Figure 15. Measured (solid line) and modeled (dash line) temperature results of TCs at TC Tree A in Case 2.....	21

Figure 16. Contour map of measured (solid line) and modeled (dash line) temperature results of crown TCs in Case 2 21

Figure 17. Representative temperature slices at: (a) $y = 3$ m, (b) $x = 2.3$ m in Case 3. Time $t = 300$ s. Temperature units are in $^{\circ}\text{C}$ 23

Figure 18. Comparison of velocity along x-axis at $y = 3$ m slice in: (a) Case 1, (b) Case 3. Time $t = 300$ s. Velocity units are in m/s 24

Figure 19. Measured (solid line) and modeled (dash line) temperature results of TCs at center along x direction (front – aft) in Case 3 24

Figure 20. Measured (solid line) and modeled (dash line) temperature results of TCs near rear burner along y direction (side – side) in Case 3..... 25

Figure 21. Measured (solid line) and modeled (dash line) temperature results of TCs at TC Tree A in Case 3..... 25

Figure 22. Contour map of measured (solid line) and modeled (dash line) temperature results of crown TCs in Case 3 26

Figure 23. Measured vs. Predicted TC temperatures averaged over the last 60 s of experiment. The three experimental cases are shown. Filled symbols represent tree thermocouples, hollow symbols crown thermocouples. Point P is an outlier value for TC56 in the rear burner Case 3. . 27

Figure 24. Average temperature contour along plane $Y = 1.73$ m (TC tree B) for Case 3. Temperatures from 22°C (blue) to 85°C (red) averaged over the last 60 sec. Thermocouples in green. The two higher thermocouples of Tree B (TC55, TC56) lay in a hot temperature region. 28

Tables

Table 1. Full-scale Fire Test Conditions.....	11
Table 2. Grid convergence thermocouple temperature norms (units in °C) for Case 1 simulation.	13
Table 3. Time averaged thermocouple temperature difference norms of experiments with respect to 2 cm grid simulations. Temperature units in °C	14

Acronyms

Acronym	Definition
AC	Advisory Circular
CAD	Computer Aided Design
CFD	Computational Fluid Dynamics
FAA	Federal Aviation Administration
FDS	Fire Dynamics Simulator
FE	Forward Euler
FV	Finite Volume
HRR	Heat Release Rate
IB	Immersed Boundary
LES	Large Eddy Simulation
LIDAR	Light Detection and Ranging Technology
MPI	Message Passage Interface
NIST	National Institute of Standards and Technology
RK2	Runge-Kutta
TC	Thermocouple

Executive summary

This study is a continuation of a previous study (Report Number: DOT/FAA/TC-18/14) where a computational fluid dynamics (CFD) tool, the Fire Dynamics Simulator (FDS), was used to simulate a small fire in the overhead inaccessible-area of a Boeing 747-SP cabin. In the modeling described in the previous report, all solid obstructions were assumed to conform to the rectangular mesh of the flow solver. It is the method of choice in regular compartments, where walls are aligned to these mesh planes. However, for non-rectangular geometries like an aircraft cabin, boundary layer phenomena become dependent on grid resolution. In this report, a new unstructured geometry capability under development in FDS at the National Institute of Standards and Technology (NIST) is employed for computer simulations. This numerical method splits Cartesian cells intersected by the surface and solves model equations on the polyhedra remaining on the fluid side. Surface meshes are defined by triangulations, a common approach in Computer Aided Design (CAD) and computational mechanics. Boundary representation is practically exact in terms of volume and area conservation, while the user is still relieved of an unstructured fluid mesh generation burden.

Fire in an aircraft overhead inaccessible-area is an ideal target for this capability, as it involves complex geometry, highly curved ceiling, and obstructions in densely cluttered spaces. It presents a challenge to aircraft fire safety and, more specifically, to timely fire detection and suppression. Fire in hidden areas must be detected at the earliest stage, which further requires better understanding of the heat and mass (including hot gases and smoke) transport within a complex area.

Therefore, the following tasks were accomplished during this research:

- Task 1: Performed full-scale fire tests at the selected region in the Boeing 747-SP cabin overhead area. Gas temperatures were measured at 50 locations.
- Task 2: Performed full-scale fire tests with reduced fire size to examine the lower limit of the model's capability to detect early fires.
- Task 3: Performed full-scale fire tests with different fire source locations to examine the model's location sensitivity.
- Task 4: Performed CFD simulations on all the test scenarios and compared the simulation results with measurements. Simulations were performed with the FDS version 6.7.4 (Git revision hash FDS6.7.4-355-ga58cb85, April 16, 2020). The FDS repository is located in <https://github.com/firemodels/fds>. The complex geometry capability is currently undergoing substantial and continuous development.

Task 5: Identified possible hot spots as a result of fire. Evaluated the accuracy in temperature magnitude prediction and fire onset time prediction using numerical methods.

CFD is found in average to predict the temperature field to within 10% of the measurements (5 °C in temperature increases of 70 °C). Reduced fire size decreases the crown temperature accordingly, without affecting the hot spot locality. New hot spots are formed with different burner locations. The ribs on the crown do not present a hindering effect on the hot gas transport across the area, but do have an influence on crown temperatures close to the fire source. The results from the current study can be used to guide the placement and certification of fire detectors and temperature sensors in transport and cargo aircraft. In addition, the test and simulation results assist in the validation of FDS.

1 Introduction

The Federal Aviation Administration (FAA) Advisory Circular (AC) 120-80A (AFS-200, December 2014) defines hidden fires as those that are not readily accessible, may be difficult to locate, and are highly challenging to extinguish. An in-flight fire in the hidden areas can be catastrophic and therefore it must be detected at its earliest stage. It is found that visual observation of major fire signatures, such as flame luminance and smoke, is usually delayed and less reliable in hidden areas. Causes of in-flight fires include wiring failures, electrical component failures, lightning strikes, and overheating of batteries. For instance, in 2013, a composite fuselage Boeing 787 operated by Ethiopian Air experienced a battery-initiated fire in the overhead space that propagated along the crown of the airplane for a considerable distance (Conradi, February 2015). Fortunately, the aircraft was on the ground and no passengers were on board, but the fire damage extended over an area of approximately 9.5 m² of the structural fuselage crown skin and fuselage frames.

In general, the hidden areas in the aircraft overhead cabin involve complex geometry, a highly curved fuselage, and densely cluttered ducts. These complexities present a great challenge for timely fire detection and suppression. Notably, there is a lack of understanding of how hot gases are transported along the curved fuselage, and how obstructions affect the flow and in turn the placement of fire detectors. Therefore, in order to provide better justification and guidance for the placement of fire detectors in overhead hidden areas, performance based full-scale studies are needed to reveal the heat and mass transfer behavior under these conditions.

In recent years, fire models based on computational fluid dynamics (CFD) have been developed, allowing for the simulation of complex fire scenarios and assisting in performance-based design of fire protection systems. Validation of these tools for scenarios where they will be used is fundamental to their reliability.

One such fire model is the Fire Dynamics Simulator (FDS) (McGrattan, et al., Fire dynamics simulator, technical reference guide, September 2013), which is used in the design of fire protection systems and the forensic reconstruction of actual fires. FDS is a large eddy simulation (LES) solver of the low Mach number approximation of fluid momentum and energy equations for a multicomponent mixture (McDermott R. J., 2014). It includes models for combustion and radiation heat transfer as well as a variety of features for fire protection engineering applications. FDS uses rectilinear meshes and a finite difference spatial discretization of the governing equations. Solid obstructions are made to conform to the numerical grid. This is a natural choice for regular compartments, where walls are generally aligned with the rectilinear grid, but it also

implies that curved geometries depend on the grid resolution. Recently, substantial work has been performed in adding to FDS the capability of representing complex geometry with surfaces defined by unstructured triangulations that do not conform to the fluid grid. Some target applications of this added functionality are fires in aircraft and transport vehicle cabins, structures with curved roofs, and outdoor fire and contaminant dispersion across complex terrains.

The key components of this new capability are a cut-cell method (Berger, 2017) to model mass and energy transport near boundaries, and an Eulerian direct forcing immersed boundary method (Fadlun, Verzicco, Orlandi, & Mohd-Yusof, 2000) (Balaras, 2004) coupled with dynamic boundary layer modeling for momentum transport (McDermott & Vanella). The cut-cells conform to the surface triangulation, rendering very precise boundary conditions and integrals. Further, small cut-cells are dealt with on explicit time integration using cell-linking to larger surrounding cells (Kirkpatrick, Armfield, & Kent, 2003). As will be discussed later, the implementation allows for parallel computations using hundreds of cores by means of the message passage interface (MPI) standard (Gropp, Lusk, & Skjellum, 1999). A fundamental aspect of scientific computing software, and of most importance to FDS development, is the verification and validation of the different physics code units, both individually and in concert. Therefore, the temperature measurements obtained from the Boeing 747 inaccessible-area experiments are used to perform validation comparisons. The behavior of the new complex geometry unit on this critical set of target scenarios is also assessed.

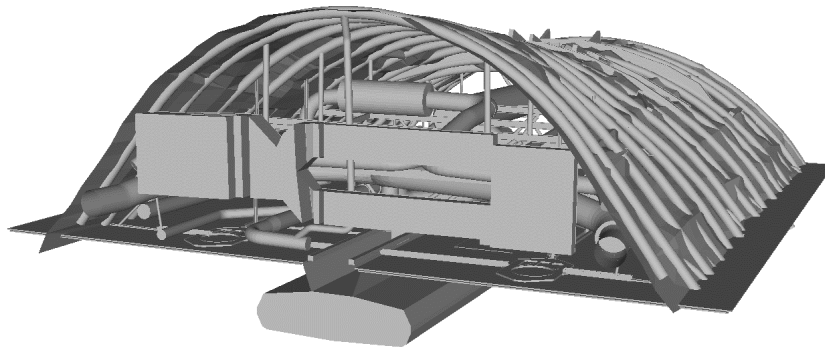
2 Experimental method

The full-scale experiment was performed in the overhead area of a Boeing B747-SP located at the FAA's William J. Hughes Technical Center. Figure 1 (a) highlights the region of interest in the test article, located at the aft of the upper deck. This region is 6.7 m long, 5.4 m wide, and 2 m tall at its highest point and decreases aft. The ribs are located every half meter. The contents of the overhead space include air-distribution ducts, cables, electrical wiring, and support structures. The front side is sealed with plastic membrane. The rear side of the highlighted area is open to the rest of the overhead region.

To reconstruct the interior geometry for CFD modeling, light detection and ranging technology (LIDAR) was used to generate a high-resolution point cloud and was then converted to a three-dimensional model. The LIDAR generated CAD model is shown in Figure 1 (b).



(a) B747-SP



(b) LIDAR generated 3-D model

Figure 1. Diagram of the full-scale test article: (a) Boeing B747-SP with highlighted overhead area, (b) LIDAR generated 3-D model

Even though aircraft fire incidents are typically associated with solid fuels (e.g. plastics or composites), a gas burner fueled with propane was used as a fire source in the full-scale experiment. The gas burner is 18 cm square and 21 cm in height. It is filled with sand to provide uniform flow. A mass flow controller (Alicat: MC-20SLPM) is used to adjust the flow rate for the desired heat release rate. Two burner locations are examined, with their relative locations marked in the plan view of the crown in Figure 2 (a). The front burner center is 1.2 m from the front insulation and 1.9 m from its closest edge; and the rear burner center is 3.7 m from the front insulation and 2.1 m from its closest edge.

To map out the hot gas movement and temperature distribution at the fuselage, the overhead area is equipped with fifty Type-K thermocouples. These thermocouples were installed on the ribs and were positioned 5 cm below the insulated crown of the fuselage. Figure 2 (a) shows the location of the thermocouples on the curved fuselage. Adjacent thermocouples are spaced 0.5 m apart. The first row of thermocouples is 0.46 m from the front. Near the left and right boundaries, thermocouples 41/42 and 49/50 are 0.67 m from the edges. Temperature contour planes in

longitudinal x , and lateral y directions used in the results section are also shown. Figure 2 (a) marks the thermocouple tree (A and B) locations, both of which are 0.4 m away from the burner center. The two thermocouple trees move with the burner location. Each thermocouple tree has four thermocouples, with the top one 5 cm below the crown of the fuselage and a 15 cm separation distance between thermocouples. The layout of thermocouples on one representative thermocouple tree is shown in Figure 2 (b).

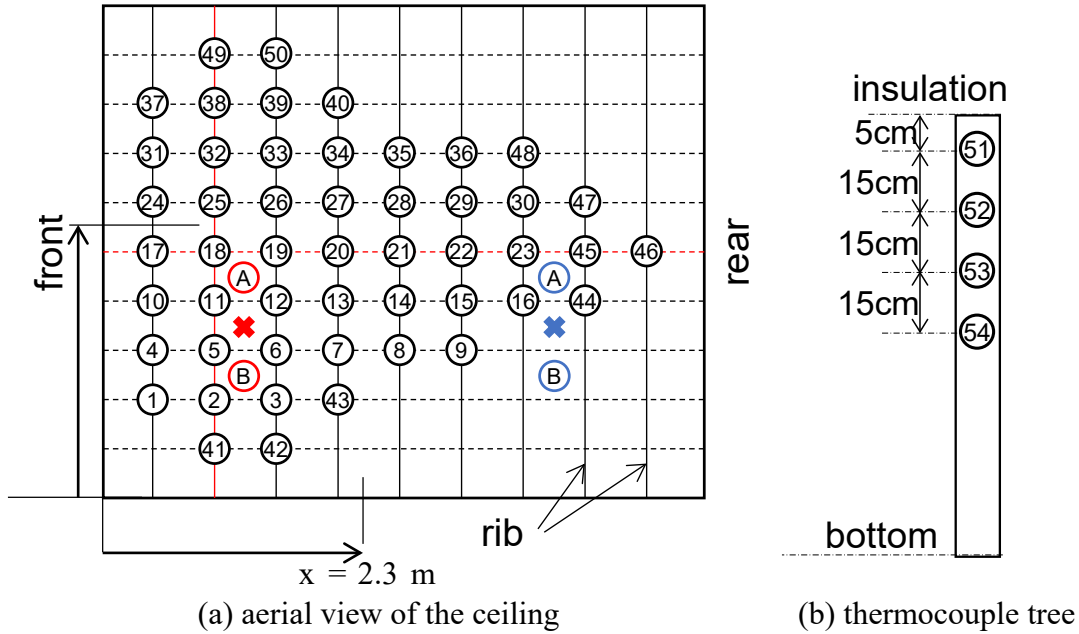


Figure 2. Detailed layout of burner, thermocouple, and thermocouple tree: (a) aerial view of the crown of fuselage, (b) side view of one representative thermocouple tree

3 Numerical method

This section describes the cut-cell immersed boundary scheme used to represent non-grid-aligned geometries in FDS. This method modifies the solution only in cells close to the geometry surfaces. It allows for FDS structured meshes to be maintained in a natural manner, implementing the new capability as an add-on.

3.1 Cut-cell method for scalar transport and energy

Consider a set of gaseous, reacting chemical species $\alpha = 1, \dots, N$ flowing on a fixed spatial domain $\Omega - \sum \Omega_i \in \mathbb{R}^n, n = 2, 3$. The regions $\Omega_i, i = 1, \dots, nbods$ correspond to immersed solid bodies. The fluid region boundary is given by the surfaces $\partial\Omega, \partial\Omega_1, \dots, \partial\Omega_{nbods}$. These species are transported on a given point \mathbf{x} in space with a mass weighted average velocity $\mathbf{u}(\mathbf{x}, t)$. In

addition, the species α density is $\rho_\alpha(\mathbf{x},t) = \rho(\mathbf{x},t) Y_\alpha(\mathbf{x},t)$, ρ is the mixture density and $Y_\alpha = \rho_\alpha / \rho$ its mass fraction. We define the convective and diffusive fluxes per unit time and area, as:

$$\mathbf{J}_{c\alpha} = \rho Y_\alpha \mathbf{u} \quad 1$$

$$\mathbf{J}_{d\alpha} = -\rho D_\alpha \nabla Y_\alpha \quad 2$$

where Fick's Law for binary diffusion with respect to a most abundant, background species has been used on the last equation. With definitions 1 and 2 the species convection-diffusion reaction mass balance equations based on mass fractions used in FDS are:

$$\frac{\partial \rho Y_\alpha}{\partial t} + \nabla \cdot (\rho Y_\alpha \mathbf{u}) = \nabla \cdot (\rho D_\alpha \nabla Y_\alpha) + \dot{m}_\alpha''', \alpha = 1, \dots, N \quad 3$$

in Ω , where $\dot{m}_\alpha'''(\mathbf{x}, t)$ is the chemical reaction volume source (sink if negative) for species α . Mass flux or composition boundary conditions are prescribed on $\partial\Omega$, $\partial\Omega_1$, ..., $\partial\Omega_{nbods}$. FDS uses staggered structured Cartesian grids, flux limited interpolation and finite differences to evaluate fluxes 1 – 2, respectively (McGrattan, et al., Fire dynamics simulator, technical reference guide, September 2013). Additionally, the so-called thermodynamic divergence is used as a proxy for the energy equation. Under the fractional step time discretization of the Low Mach approximation for the Navier Stokes equations, this energy derived divergence is imposed on the evolving mixture velocity field (McGrattan, et al., Fire dynamics simulator, technical reference guide, September 2013) (McDermott R. J., 2014). Starting from the sensible enthalpy evolution equation, the divergence of the velocity field can be factored as (McDermott R. J., 2014):

$$\begin{aligned} (\nabla \cdot \mathbf{u})^{th} = & \left[\frac{1}{\rho c_p T} - \frac{1}{\bar{p}} \right] \frac{\partial \bar{p}}{\partial t} + \frac{w \rho_0 g_z}{\rho c_p T} + \frac{1}{\rho c_p T} [\dot{q}''' - \nabla \cdot \dot{\mathbf{q}}'' - \mathbf{u} \cdot \nabla(\rho h_s)] + \\ & \frac{1}{\rho} \sum_{\alpha} \left(\frac{\bar{W}}{W_\alpha} - \frac{h_{s,\alpha}}{c_p T} \right) [\dot{m}_\alpha''' - \nabla \cdot \mathbf{J}_{d\alpha} - \mathbf{u} \cdot \nabla(\rho Y_\alpha)] \end{aligned} \quad 4$$

where h_s is the local sensible enthalpy, \dot{q}''' is the heat release rate due to combustion, $\dot{\mathbf{q}}''$ is the heat flux, sum of conduction, convection and radiation, and \bar{p} and T are the background pressure and local temperature on the Low Mach number approximation adopted. The mixture specific heat at constant pressure and molecular weight are $c_p = \sum_{\alpha=1}^N c_{p,\alpha} Y_\alpha$ and $\bar{W} = (\sum_{\alpha=1}^N Y_\alpha / W_\alpha)^{-1}$ respectively, built from the individual species counterparts as defined. Finally, w , ρ_0 , g_z on the stratification term are respectively, the local vertical velocity, density for standard conditions (depends on vertical coordinate), and gravity acceleration.

In Figure 3, a sphere is defined by its surface triangulation within an FDS mesh. Some Cartesian cells and faces belonging to this mesh are traversed by the object surface. Gasphase cut-cells and cut-faces are named as the polyhedra and polygons that lay within their Cartesian counterparts and define regions outside the solid. See Figure 3 (b) involving an immersed c-shaped beam. In this figure, it is also noted that a two level of refinement grid hierarchy emerges. The coarse level is defined by the Cartesian entities, whereas the fine level is defined by the cut-cell or unstructured counterparts. The final grid system is composed of regular cells away from the immersed bodies and cut-cells surrounding these. Methods that evolve governing equations on these grids are called cut-cell or embedded boundary methods (Berger, 2017).

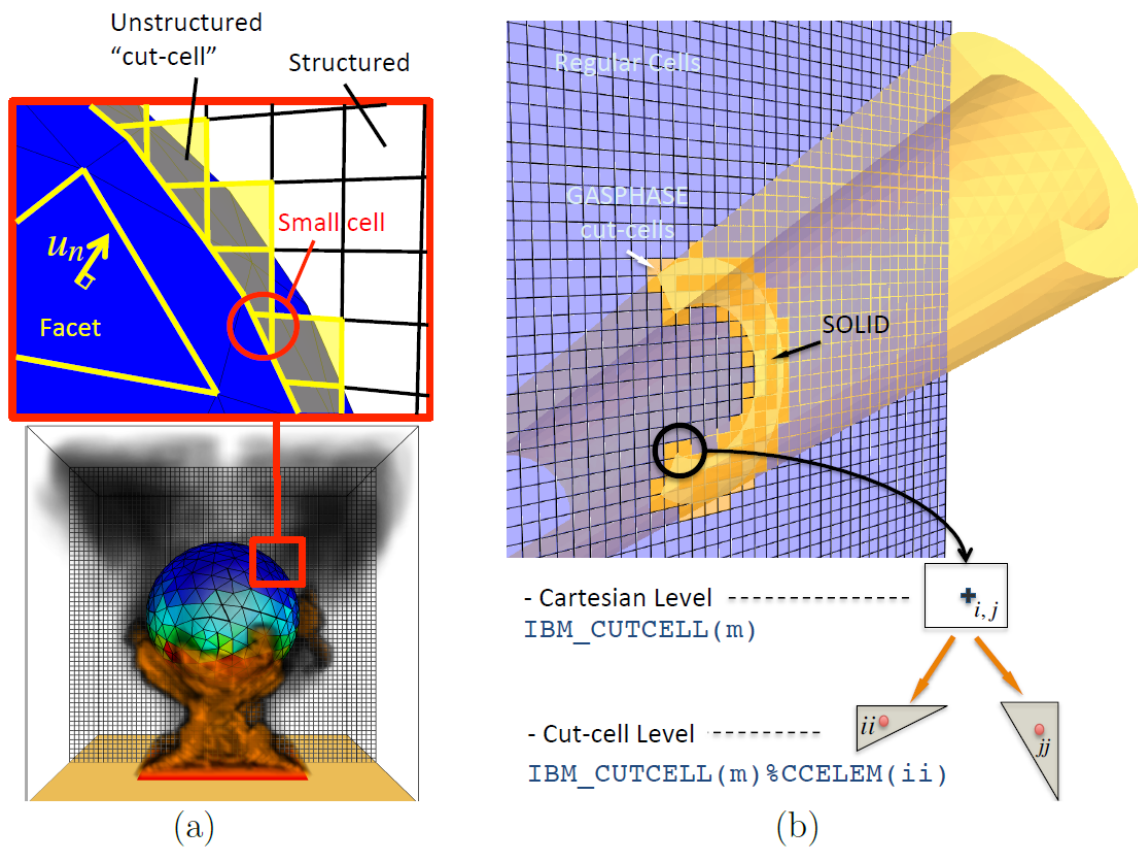


Figure 3. Regular Cartesian and cut-cell grids: (a) Cut-cell region defined around triangulated spherical surface, (b) Cut-cells defined from C-shaped beam, and 2 refinement level interpretation

In order to keep the description concise, it is assumed that the cut-cells and their geometry properties can be computed in a robust and accurate manner (a whole subject in itself) and the finite volume (FV) discretization of scalar transport and thermodynamic divergence in these cut-cells can be described. In FDS the scalar transport equations are discretized by the finite volume

method (LeVeque, 2002) (Eymard, Gallouet, & Herbin, 2000). Considering the integral form of equation 3 over a cell control volume Ω_{ii} , see Figure 4 (a), for a given cell ii (in this case a cut-cell):

$$\int \frac{\partial \rho Y_\alpha}{\partial t} d\Omega + \int \nabla \cdot (\mathbf{J}_{c\alpha}) d\Omega = - \int \nabla \cdot (\mathbf{J}_{d\alpha}) d\Omega + \int \dot{m}_\alpha''' d\Omega \quad 5$$

Assuming a time independent control volume, the time derivative and source terms are approximated by

$$\int \frac{\partial \rho Y_\alpha}{\partial t} d\Omega = \frac{\partial}{\partial t} \int \rho Y_\alpha d\Omega = \frac{\partial \bar{\rho Y}_{\alpha ii}}{\partial t} V_{ii} \quad 6$$

$$\int \dot{m}_\alpha''' d\Omega = \bar{\dot{m}}_{\alpha ii}''' V_{ii} \quad 7$$

where V_{ii} is the volume of cell ii and tildes imply cell averages. To discretize both diffusive and advective terms in equation 5, the divergence theorem is used. In the following the tildes are dropped to simplify the notation, keeping in mind that using FV, quantities will always be cell or face averaged. Consider the FV discretization of the diffusive term (equation 5 on cut-cell ii of Figure 4 (a)):

$$\int \nabla \cdot (\mathbf{J}_{d\alpha}) d\Omega = \int (-\rho D_\alpha \nabla Y_\alpha) \cdot \hat{\mathbf{n}}_{ii} d\partial\Omega = \sum_{k=1}^{n_{fc}=6} (-\rho D_\alpha \nabla Y_\alpha)_k \cdot \hat{\mathbf{n}}_{ii,k} A_k \quad 8$$

The integral over the cut-cell volume has been transformed in an area integral on its six faces. As these k faces are planar with normal outside $\hat{\mathbf{n}}_{ii,k}$ and area A_k , the method for evaluation of mean diffusive fluxes $(-\rho D_\alpha \nabla Y_\alpha)_k$ on these will define the spatial accuracy of the discretization. A simple centroid to centroid (i.e. Δy_{cc} in Figure 4 (a)) finite difference and linear interpolation is used to approximate ∇Y_α and ρD_α for each face belonging to the gas phase. In addition, a normal probe approach (Balaras, 2004) is used to sample information from the fluid to define fluxes in boundary cut-faces.

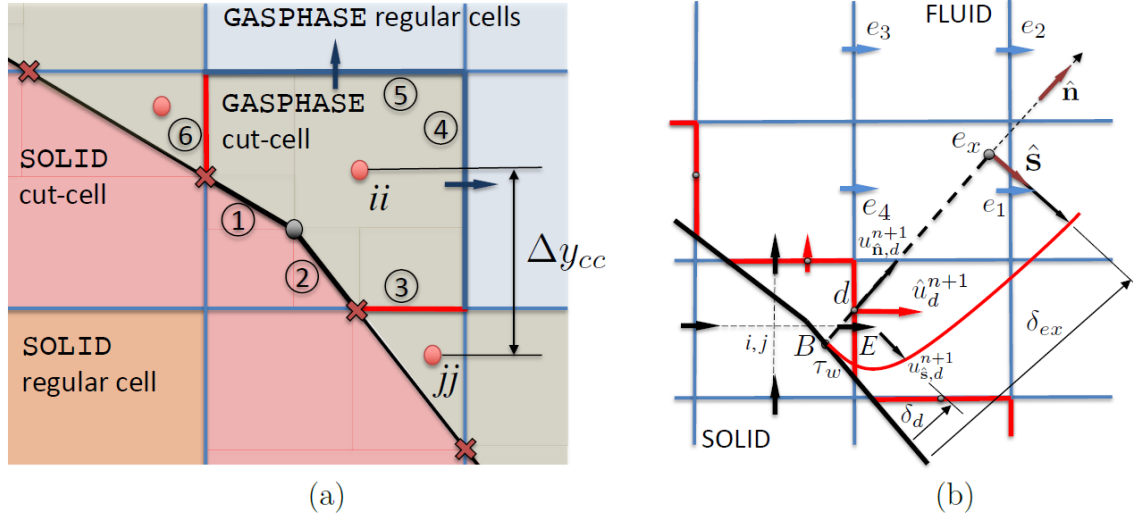


Figure 4. Cut-cell and faces in 2D: (a) Cut-cell ii surrounded by gas phase regular and cut-faces (3-6), and boundary cut-faces (1-2). (b) Interpolation sketch for wall modeled immersed boundary reconstruction of cut-face velocities

Similarly, for the advective term:

$$\int \nabla \cdot (\mathbf{J}_{c\alpha}) d\Omega = \int (\rho Y_\alpha \mathbf{u}) \cdot \hat{\mathbf{n}}_{ii} d\partial\Omega = \sum_{k=1}^{n_{fc}} (\rho Y_\alpha \mathbf{u})_k \cdot \hat{\mathbf{n}}_{ii,k} A_k \quad 9$$

where the advective flux for face k is $(\rho Y_\alpha \mathbf{u})_k = \overline{[\rho Y_\alpha]_k} \mathbf{u}_k$, and the over bar means it is a flux limited interpolation to the cut-face (McGrattan, et al., Fire dynamics simulator, technical reference guide, September 2013). In the cut-cell region Godunov interpolation is used for the advective term. As the time integration scheme in FDS is an explicit Runge-Kutta (RK2) method, all variables in the right-hand side of equations 8 and 9 are assumed known. The FV counterpart of the thermodynamic divergence expression for cut-cell ii can also be defined. For each RK2 substep, the species transport equations are advanced in all FDS Cartesian cells, and then the solution (explicit fluxes and scalar densities) are recomputed on the unstructured cut-cell region. A similar procedure is done for the thermodynamic divergence. The momentum equations and pressure Poisson equation are solved in the Cartesian mesh. Therefore, an immersed boundary method is used to reconstruct velocities in the cut-cell region.

3.2 Immersed boundary method on cut-cell region and wall model

Consider the Newtonian flow problem defined by the following set of partial differential equations (McGrattan, et al., Fire dynamics simulator, technical reference guide, September 2013):

$$\frac{\partial \mathbf{u}(\mathbf{x}, t)}{\partial t} = -[\mathbf{F}(\mathbf{u}, \mathbf{x}, t) + \nabla H(\mathbf{x}, t)], \mathbf{x} \in \Omega - \sum \Omega_i, t \in \mathbb{R}_+ \quad 10$$

$$\nabla \cdot \mathbf{u}(\mathbf{x}, t) = (\nabla \cdot \mathbf{u})^{th} \quad 11$$

where equation 10 is the momentum equation, $\mathbf{u}(\mathbf{x}, t)$ is the spatial velocity field, $\mathbf{F}(\mathbf{u}, \mathbf{x}, t)$ is a vector containing convective, diffusive and possibly other force terms, and $H(\mathbf{x}, t)$ is a potential scalar field (physically the head field in this case, commonly called pressure). Boundary conditions are prescribed for $\mathbf{u}(\mathbf{x}, t)$ on $\partial\Omega, \partial\Omega_1, \dots, \partial\Omega_{nbods}$. Classical fractional step methods for time integration of incompressible or low Mach flow are based on two operations: first, momentum transport to obtain intermediate velocities, and second, projection of velocities into a target divergence space. Consider the Forward Euler (FE) update of the governing equations from t_n to $t_{n+1} = t_n + \Delta t$ of the form: Given $\mathbf{u}^n = \mathbf{u}(\mathbf{x}, t_n)$, $\nabla \cdot \mathbf{u}^{n+1} = (\nabla \cdot \mathbf{u}^{n+1})^{th}$ known

$$\frac{\mathbf{u}^{n+1} - \mathbf{u}^n}{\Delta t} = -[\mathbf{F}^n + \nabla H^n] \quad 12$$

$$\nabla \cdot \mathbf{u}^{n+1} = (\nabla \cdot \mathbf{u}^{n+1})^{th} \quad 13$$

where \mathbf{u}^{n+1} represents a numerical approximation to the solution in equations 10 and 11 at time t_{n+1} . This discrete FE update corresponds to the first sub-step of the FDS explicit RK2 integrator. As the potential field $H(\mathbf{x}, t)$ does not have a time evolution equation, it is assumed responsible for enforcing the divergence condition and used on the projection step. Taking the divergence of equation 12 and considering the constraint 13, the two steps of the method are

1. Solve Poisson equation for H^n :

$$\nabla \cdot \nabla H^n = - \left[\frac{(\nabla \cdot \mathbf{u}^{n+1})^{th} - \nabla \cdot \mathbf{u}^n}{\Delta t} \right] - \nabla \cdot \mathbf{F}^n \quad 14$$

2. Obtain final velocity for step:

$$\mathbf{u}^{n+1} = \mathbf{u}^n - \Delta t [\mathbf{F}^n + \nabla H^n] \quad 15$$

The term $\hat{\mathbf{u}}^{n+1} = \mathbf{u}^n - \Delta t \mathbf{F}^n$ is known as intermediate velocity, and is a non-divergence-matching approximation to \mathbf{u}^{n+1} (i.e. $\nabla \cdot \hat{\mathbf{u}}^{n+1} \neq (\nabla \cdot \mathbf{u}^{n+1})^{th}$). A consequence of the projection scheme is that boundary conditions are required on the Poisson equation of step 1 (equation 14). For explicit methods and stationary solid boundaries, the corresponding boundary condition is homogeneous Neumann for H^n in $\partial\Omega, \partial\Omega_1, \dots, \partial\Omega_{nbods}$ (Perot, 1993).

In order to approximate the no slip boundary condition for immersed solid boundaries, a direct forcing immersed boundary (IB) method is employed for the momentum equations (Fadlun, Verzicco, Orlandi, & Mohd-Yusof, 2000). In order to do this, a force field is devised on the discrete momentum equations on grid faces crossed by the immersed surfaces, to approximate the no-slip boundary condition on said surfaces, while dynamically modeling the surrounding velocity field (McDermott & Vanella). In Figure 4 (b), the velocity update in each of the gas phase cut-face centroids d is done individualizing the point B on the boundary and normal direction through these centroids. In addition, an external point e_x through the normal $\hat{\mathbf{n}}$ is defined at a distance δ_{ex} , of the order of the Cartesian cells size. Known velocities and fluid parameters at time step n are interpolated from the surrounding fluid points e_1, \dots, e_4 to e_x . This information is used to estimate the stress at the wall τ_w at point B, assuming the log law equilibrium boundary layer solution (McGrattan, et al., Fire dynamics simulator, technical reference guide, September 2013). Then, a target velocity at step $n+1$, \hat{u}_d^{n+1} is dynamically estimated through a single step integration of the streamwise-normal boundary layer equations. The target velocity \hat{u}_d^{n+1} component on the cut-face centroid is flux matched to the under-lying Cartesian face E velocity component \hat{u}_E^{n+1} . Finally, an immersed boundary force

$$F_E^k = -\frac{\hat{u}_E^{n+1} - u_E^n}{\Delta t} - \frac{\partial H^{n,k-1}}{\partial x} \quad 16$$

can be computed and used in equation 14 to take into account the presence of the body. The index k refers in this context to the sub-iteration that can be performed in the IB force 16 and projection 14 - 15 to match final velocities with the dynamically estimated targets.

4 Boeing 747 overhead inaccessible-area validation cases

In this section, details of the fire scenarios are presented. Their corresponding simulation setups and simplification are introduced. In addition, the grid convergence is also discussed to ensure consistent behavior of simulations with mesh size.

4.1 Fire scenarios

Three full-scale fire tests are performed; each has 2-3 replicates to ensure consistency. Each fire test lasts 5 min, plus 30 s steady baseline before ignition. The replicate temperature results are then averaged. Details of the test scenarios are summarized in Table 1. Case 1 is a repeat of the test in a previous study (Guo, Oztekin, Crowley, Scrofani, & Lyon, February 2019). Propane flow rate is regulated at $0.24 \text{ g/s} \pm 0.0014 \text{ g/s}$ (0.6 % flow controller uncertainty reported by manufacturer), yielding a constant heat release rate of $11 \text{ kW} \pm 0.07 \text{ kW}$. The heat release rate

(HRR) matches that of FAA’s standard fire source (polyurethane foam block). It is our objective to explore the system’s limit in detecting fire at the earliest stage. Therefore, a reduced fire size is also desired to produce a slower temperature-rise. In Case 2, a reduced fire size of $5.5 \text{ kW} \pm 0.03 \text{ kW}$ is used. In both Cases 1 and 2, the front burner location has a higher crown height (as indicated in Figure 1) where the hot gases move to. However, when considering the obstruction presented by ribs along the crown of the fuselage, it is not clear if the hot gases produced in the rear burner location can migrate to higher crown areas. In Case 3, the burner location is moved to the rear part of the overhead area. The center of the front burner is 1.25 m away from the front panel and 2 m from the near edge. The center of the rear burner is 3.75 m away from the front panel and 2.25 m from the near edge.

Table 1. Full-scale Fire Test Conditions

	Fire Size	Burner Location	Ambient Temperature
Case 1	11 kW	Front	28 °C
Case 2	5.5 kW	Front	28 °C
Case 3	11 kW	Rear	22 °C

4.2 Simulation setup

Large eddy simulations (LES) are performed in FDS for the fire tests of interest. The overhead inaccessible-area is defined by triangulations representing the piping, roof insulation and structural members. A total of 153,000 vertices and 306,000 triangles are used to define the geometries (see Figure 5). Cell sizes of 6 cm, 4 cm, and 2 cm are tested in the simulations. For the finest mesh, ten cells span the burner width. The number of meshes and MPI processes varies from 12 for the coarser grids, and up to 189 in the fine 2 cm grid cases. This corresponds to about 9 million total computational cells through 144 MPI processes for the overhead area, plus 45 MPI processes for the extension area.

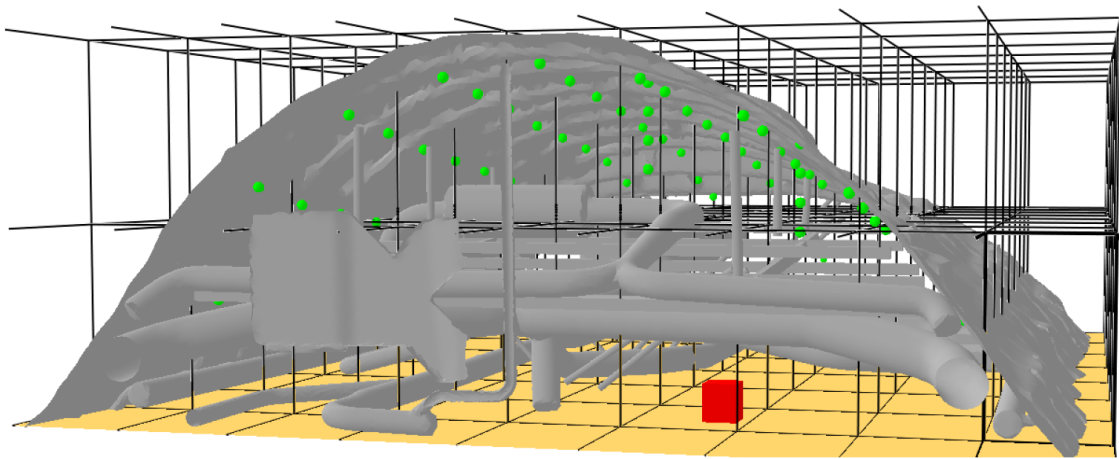


Figure 5. Front burner model setup: Overhead inaccessible-area surfaces in grey and burner defined in red. Roof and tree thermocouples are defined in green. Modeled region is divided in 144 FDS fluid meshes (black wireline) for fine grid cases.

The ambient temperature in the model is set to be consistent with the measured initial temperature on the test day. The ambient pressure in the model is set to be 100 kPa. Propane is specified as fuel in FDS model, with its heat of combustion specified as 46.36 kJ/g, and its soot yield specified as 0.02.

In the overhead area, different insulation materials are applied to the fuselage blanket and ducts, but the thermal properties of these materials are not readily available. The regions close to the high temperature zone are hardened with ceramic paper. In the model, only the ceramic paper property is applied to the insulated surfaces, sufficient to capture most of the heat loss through the surfaces. The ceramic paper insulation properties are as follows: specific heat $c_p = 1$ kJ/kg·K, thermal conductivity $\kappa = 0.05$ W/(m·K), density $\rho = 192$ kg/m³, and thickness $d = 1.5$ mm. Thermocouples are modeled in the FDS simulation employing the following parameters: bead emissivity 0.8, density 8600 kg/m³, diameter 0.5 mm, and specific heat 0.523 kJ/(kg·K), consistent with the Type-K sensors used in experiments. Thermocouple readings are averaged in 5 s time intervals in both experiments and simulations.

The computational domain is 6.7 m in length, shorter than the total length of about 20 m in the whole overhead region. In this study, one case has the rear burner location close to the computational domain rear boundary. To minimize the impact of this situation, the rear side is modeled as an extension of an extra length of 4.2 m. The rear boundary surface is changed from a passive opening to an insulated wall. Further, an open vent is assumed in the floor of this extension, to allow fresh air to recirculate as seen in the airplane. The front side is sealed as in the experiments. Simulations are run for 300 s. These calculations take between a few hours

(coarse cases) to 72 hours for the fine 2 cm grid cases on an Intel Xeon@CPU E5-2630 computing cluster.

Measures of grid convergence in the form of average, root mean square (*rms*) and maximum temperature differences from the finest grid simulation over the 50 crown thermocouples are chosen for the Case 1 setup. Time averaging is performed over the second half of the simulation for these measures. Then,

$$|\bar{T}_g - \bar{T}_{2cm}|_{avg} = \frac{1}{50} \sum_{k=1}^{50} |\bar{T}_{k,g} - \bar{T}_{k,2cm}| \quad 17$$

$$|\bar{T}_g - \bar{T}_{2cm}|_{rms} = \sqrt{\frac{1}{50} \sum_{k=1}^{50} |\bar{T}_{k,g} - \bar{T}_{k,2cm}|^2} \quad 18$$

$$|\bar{T}_g - \bar{T}_{2cm}|_{\infty} = \max_{k=1, \dots, 50} |\bar{T}_{k,g} - \bar{T}_{k,2cm}| \quad 19$$

quantify the difference of solution on grid g with respect to the fine 2 cm grid, k refers to the thermocouple number, and the over-line in \bar{T} refers to a time averaged temperature. In Table 2, 6 cm and 4 cm grids thermocouples results are compared to the fine 2 cm grid computation. It is seen that all difference measures decrease as the grid is refined, showing a difference of about two degrees in average and *rms* thermocouple temperatures between the 4 cm and 2 cm grids. The maximum difference seen is about 9 °C. In the following section, comparisons of the 2 cm calculations with respect to experiments are presented.

Table 2. Grid convergence thermocouple temperature norms (units in °C) for Case 1 simulation.

Grid	$ \bar{T}_g _{\infty}$	$ \bar{T}_g - \bar{T}_{2cm} _{avg}$	$ \bar{T}_g - \bar{T}_{2cm} _{rms}$	$ \bar{T}_g - \bar{T}_{2cm} _{\infty}$
6 cm	86.6	6.3	7.0	14.0
4 cm	97.7	1.7	2.2	9.3
2 cm	95.9	/	/	/

5 Results

Both measured and modeled temperature results from the three fire scenarios are presented in this section. Figure 6(a) shows a photo of the established fire on top of the gas burner in Case 1. The Smokeview (Forney, 2020) rendering of the modeled results in Case 1, including a

temperature slice at $y = 3$ m and at $t = 300$ s is exhibited in Figure 6(b). A hot zone with temperatures as high as $95\text{ }^\circ\text{C}$ at the crown of the fuselage near the fire source can be identified.

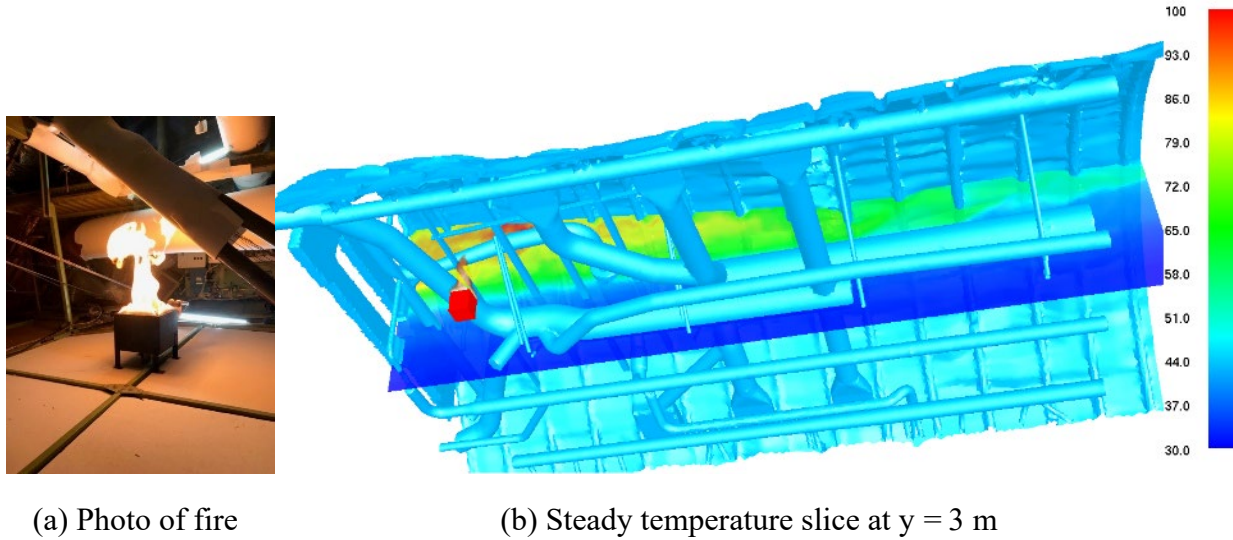


Figure 6. Example fire test photo and steady state temperature slice at $y = 3$ m for Case 1

As a first validation step, the thermocouple temperature difference norms are used, as defined in the previous section. Now the fine 2 cm calculations with respect to experimental measurements for Cases 1, 2 and 3 of Table 1 are tested, see Table 3. It is found that, for all cases, average and *rms* thermocouple temperature difference norms vary between $3\text{ }^\circ\text{C}$ and $6\text{ }^\circ\text{C}$. These values lay within 5% of the maximum measured. Maximum differences are located at mid height within the hidden space. It is speculated that the large differences are due to less mixing and a sharper boundary between cold and hot layers seen in the simulations.

Table 3. Time averaged thermocouple temperature difference norms of experiments with respect to 2 cm grid simulations. Temperature units in $^\circ\text{C}$

	$ \bar{T}_{exp} _\infty$	$ \bar{T}_{2cm} _\infty$	$ \bar{T}_{exp} - \bar{T}_{2cm} _{avg}$	$ \bar{T}_{exp} - \bar{T}_{2cm} _{rms}$	$ \bar{T}_{exp} - \bar{T}_{2cm} _\infty$
Case 1	96.4	95.9	4.5	6.1	17.2
Case 2	67.8	67.9	3.1	4.0	10.2
Case 3	99.6	93.6	4.2	5.9	13.8

Next, the modeled temperature slices at $y = 3.0$ m and at $x = 2.3$ m are presented for each case. The temperature slices are rendered in Smokeview (Forney, 2020). Representative thermocouples are selected to compare the temperature history between experiments and simulations. The selected three groups of thermocouples (TCs) are:

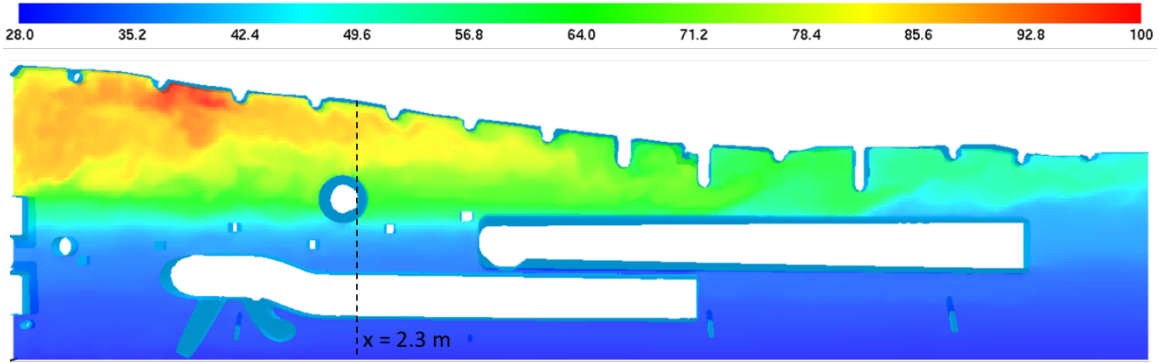
- Group 1 – TC17, TC19, TC21, TC23, TC46, located at center along the x direction (front to aft),
- Group 2 – TC05, TC18, TC32, TC41, TC49, located near front burner along the y direction (side to side),
- Group 3 – TC51, TC52, TC53, TC54, located on TC tree A.

The two axes along which the first two groups of thermocouples are located are also marked in Figure 2. In addition, temperatures during the last 10 s are averaged (representing the quasi-steady state) for the temperature contour map comparison.

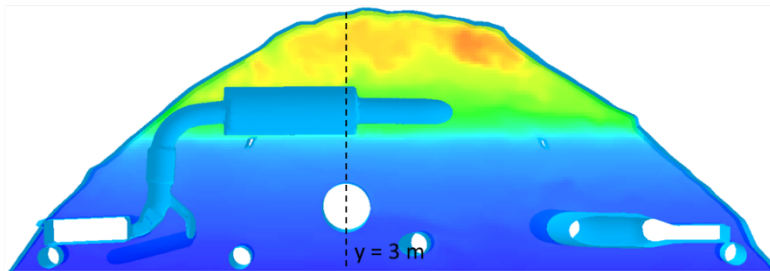
5.1 Case 1 temperatures

Figure 7 shows modeled temperature contours rendered from Smokeview in Case 1 at $t = 300$ s when the quasi-steady state is established. The relative location of x-slice is also marked on the y-slice, and vice versa. In general, there is no obvious abrupt temperature change across the ribs, indicating the ribs do not significantly hinder the flow. Higher temperatures are found in the space between ribs on the crown of the fuselage on top of the burner. The difference is about 10 °C and is also reflected in TC tree measurements. The major ducts below do not appear to have significant impact on either the flow field or heat transfer.

Figure 8 to Figure 10 present the selected three groups of thermocouple results versus time in Case 1. The solid line represents the measurements, and the dash line represents the simulations. Crown thermocouple results at 300 s (quasi-steady state) are projected onto the same plane (see Figure 2 (a)) to map the temperature distribution as shown in Figure 11. The colored contour line indicates the region having the same temperature with its temperature value specified at the right side legend. Figure 11 compares the Case 1 temperature contour at the quasi-steady state from tests (solid line) and simulations (dash line) respectively.



(a) Temperature Slice at $y = 3.0$ m.



(b) Temperature Slice at $x = 2.3$ m.

Figure 7. Representative temperature slices at: (a) $y = 3$ m, (b) $x = 2.3$ m in Case 1. Time $t = 300$ s. Temperature units are in $^{\circ}\text{C}$

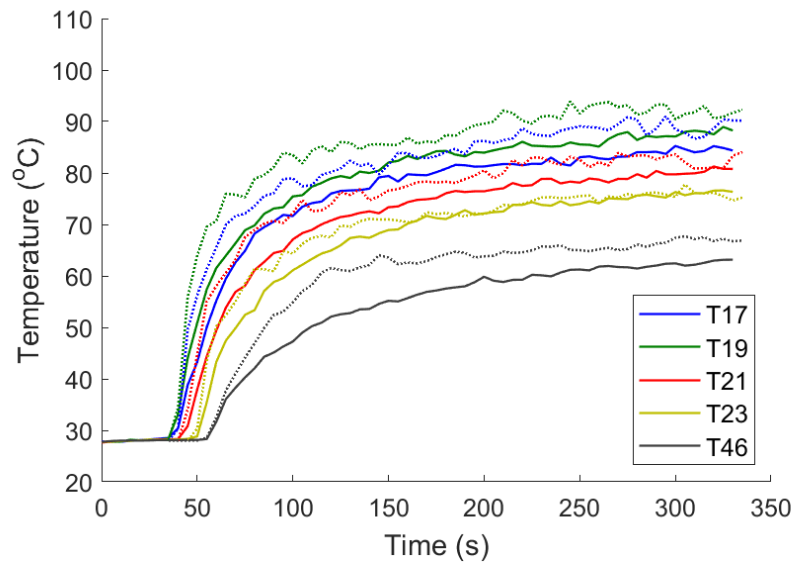


Figure 8. Measured (solid line) and modeled (dash line) temperature results of TCs at center along x direction (front – aft) in Case 1

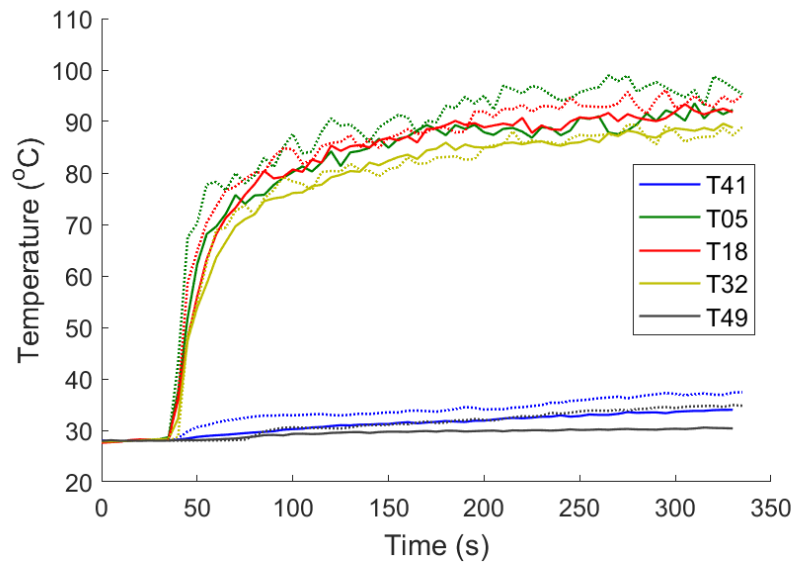


Figure 9. Measured (solid line) and modeled (dash line) temperature results of TCs near front burner along y direction (side – side) in Case 1.

For Case 1, as shown in Figure 8 and Figure 9, the model tends to slightly over-predict the temperatures, and the difference between the measured and predicted temperatures is typically 10 °C or less. Also, the timing of the temperature onsets is well captured as hot gases move along the crown of the fuselage from front to aft. It should be noted that the quasi-steady behavior in tests is also accurately predicted by the model. In both tests and models, the temperature slowly rises after 2 min. In the previous study (Guo, Oztekin, Crowley, Scrofani, & Lyon, February 2019) with an “Open” boundary specified at the rear side, steady state is quickly achieved after 2 min and the modeled temperature keeps constant over time.

In the comparison of thermocouple tree results (Figure 10), the model over-predicts the near-crown temperature (TC51) by about 10 °C. The disagreement increases as the height decreases. It is noted that unlike the rest of the fifty thermocouples that are laid underneath the ribs, the top thermocouples on TC trees (TC51 on tree A and TC55 on tree B) are directly laid underneath the crown and its physical location is actually higher than that of the surrounding rib thermocouples.

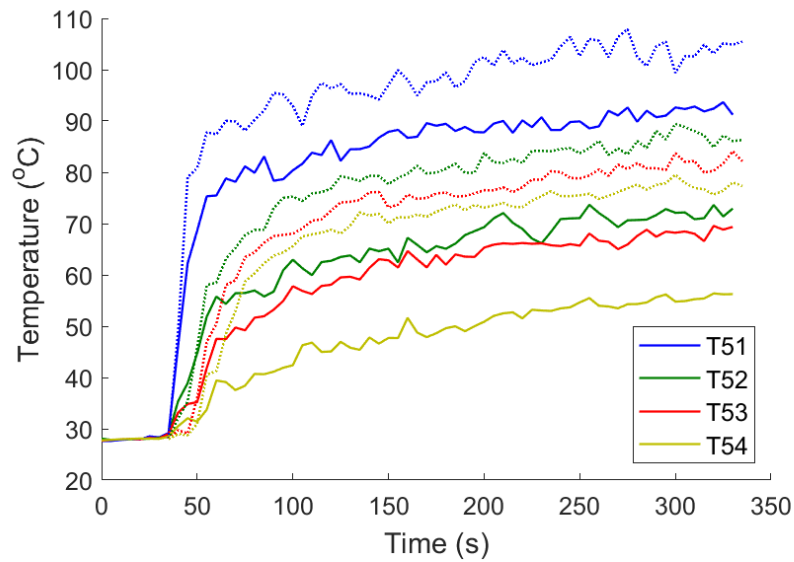


Figure 10. Measured (solid line) and modeled (dash line) temperature results of TCs at TC Tree A in Case 1.

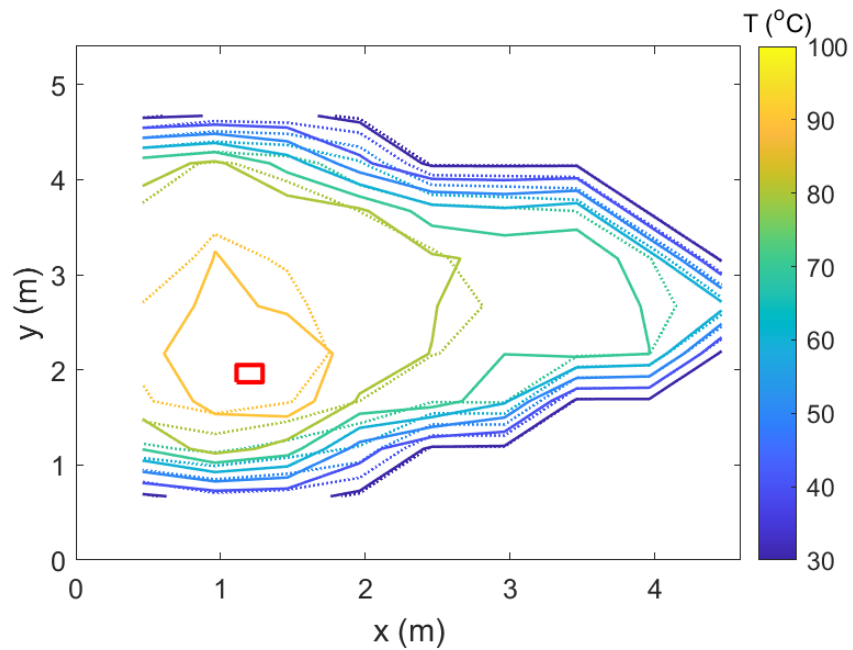


Figure 11. Contour map of measured (solid line) and modeled (dash line) temperature results of crown TCs in Case 1.

The contour plots of temperature in both experiments and models are overlaid in Figure 11. In most of the region, the contour lines are superimposed, except that in the high temperature region, the contour line of 90 °C is slightly wider in the model, indicating slight over-prediction.

5.2 Case 2 temperatures

Figure 12 exhibits representative temperature slices at $y = 3$ m and at $x = 2.3$ m, at $t = 300$ s rendered from Smokeview in Case 2. The maximum temperature in the scale is reduced by about 30 °C with respect to Case 1 due to the decreased energy release of the burner. Temperature distribution and the hot layer height is similar to that in Case 1. Figure 13 to Figure 15 display the comparison of temperature measurements, and predictions. The solid line represents measurements and the dash line represents simulations. Figure 16 compares the Case 2 temperature contour from tests and simulations respectively.

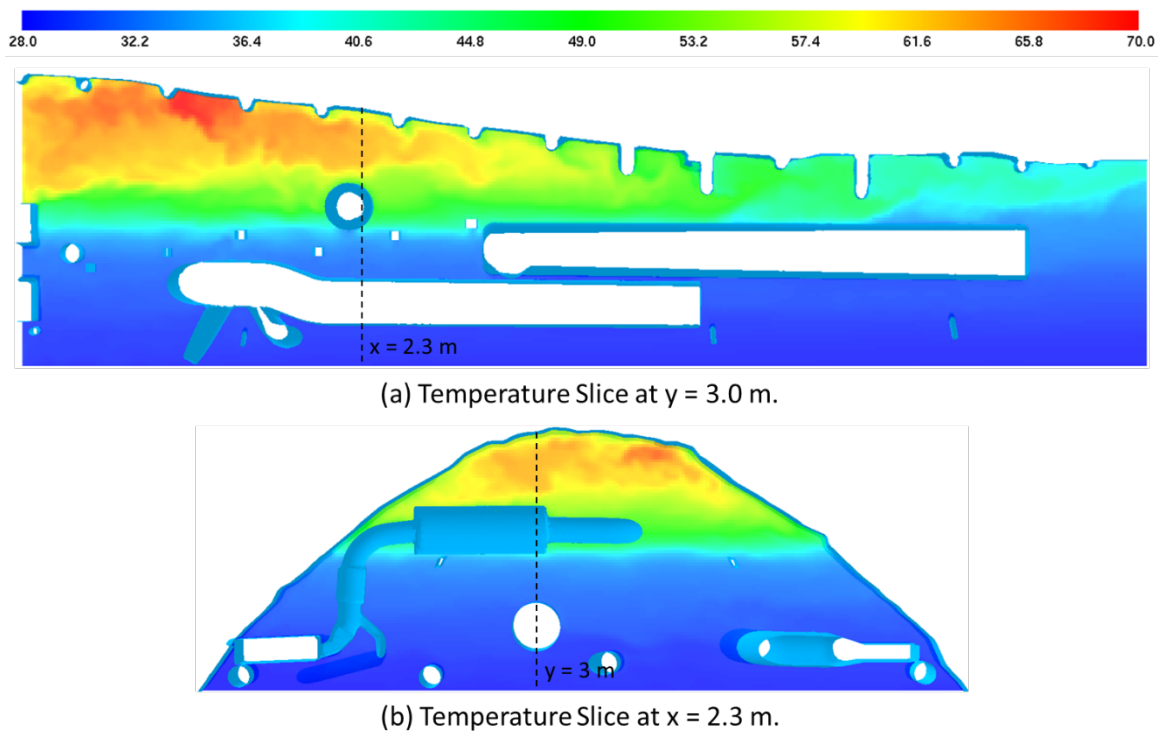


Figure 12. Representative temperature slices at: (a) $y = 3$ m, (b) $x = 2.3$ m in Case 2. Time $t = 300$ s. Temperature units are in °C

As the fire size is decreased by 50 % for Case 2 compared with Case 1, the temperature at the crown of the fuselage is reduced by about 30 °C in the high temperature region. Model over-prediction is also found as in Case 1, indicated by the larger contour lines in Figure 16. The timing of temperature onsets is well captured, and the predicted crown temperatures are in correct range. As the fire heat release rate is decreased by half, the characteristic fire size, D^* , is decreased by 24%, following (McGrattan, et al., Fire dynamics simulator, technical reference guide, September 2013):

$$D^* = \left[\frac{\dot{Q}}{\rho_\infty c p_\infty T_\infty \sqrt{g}} \right]^{2/5}$$

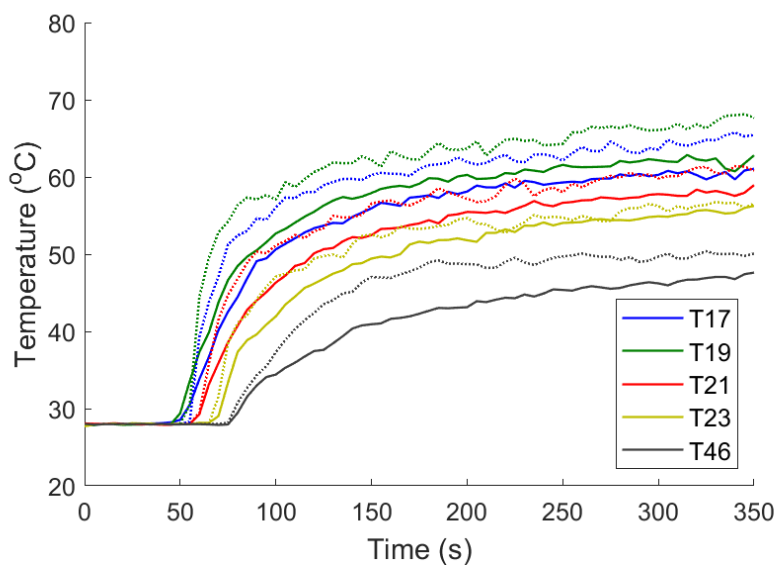


Figure 13. Measured (solid line) and modeled (dash line) temperature results of TCs at center along x direction (front – aft) in Case 2

Under this condition, the same cell size of 2 cm, which was sufficient for Case 1, is marginal in resolving buoyant plumes, which adds to the differences found for this case.

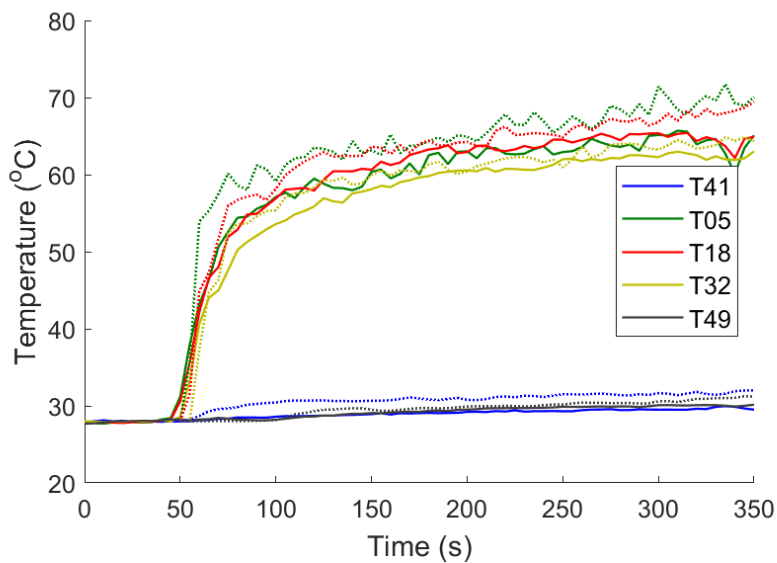


Figure 14. Measured (solid line) and modeled (dash line) temperature results of TCs near front burner along y direction (side – side) in Case 2

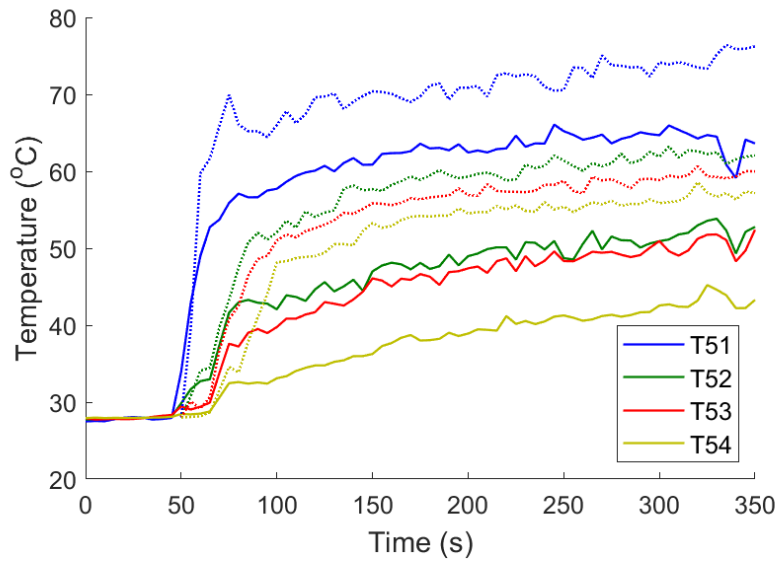


Figure 15. Measured (solid line) and modeled (dash line) temperature results of TCs at TC Tree A in Case 2

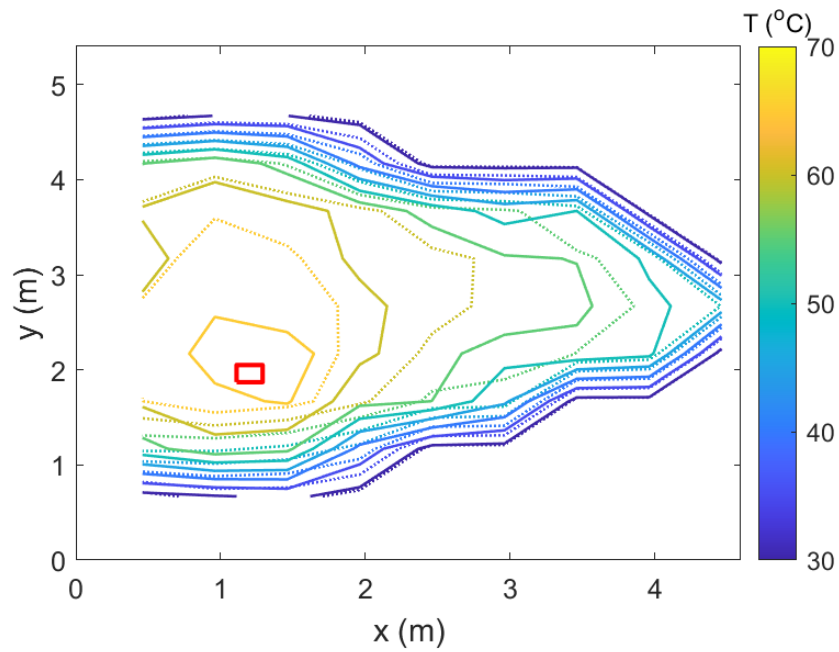
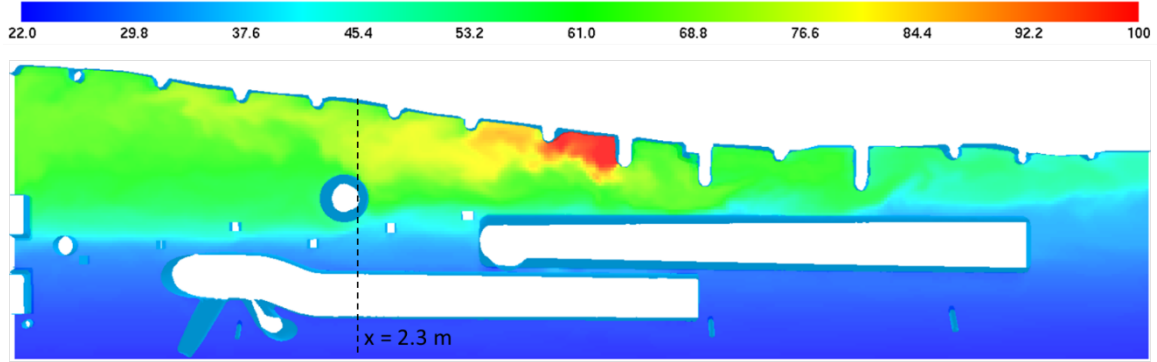


Figure 16. Contour map of measured (solid line) and modeled (dash line) temperature results of crown TCs in Case 2

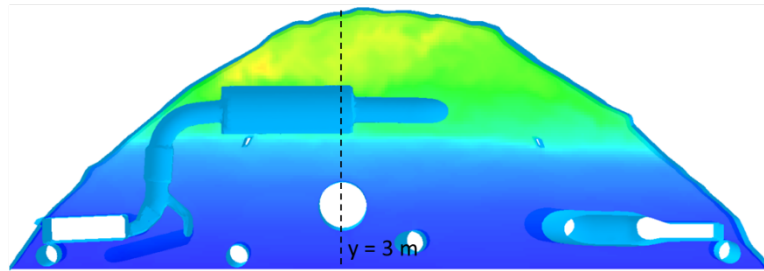
5.3 Case 3 temperatures

Figure 17 exhibits representative temperature slices at $y = 3$ m and at $x = 2.3$ m, at $t = 300$ s rendered from Smokeview in Case 3. The hot zone is confined by the two ribs adjacent to the burner. Beyond that, the heat is transported to either higher crown or aft regions. To better illustrate this phenomenon, the Smokeview slices of the x-axis velocities for both Case 1 and Case 3 are presented in Figure 18. Positive velocity indicates flow toward the aft direction, while negative velocity indicates flow toward the front location. It is seen that in Case 3, the flow velocities towards the front region are comparable to velocities towards the aft region. Figure 19 to Figure 21 present the selected three groups of thermocouple results versus time in Case 3. The solid line represents measurements from tests and the dash line represents modeled temperatures from simulations. Figure 22 compares the Case 3 temperature contour from tests and simulations respectively.

In this scenario, the fire source is closer to the rear boundary and is assumed to be affected more by the rear boundary condition and extended domain. As indicated in Figure 22, the two steady state contours almost superimpose except that the high temperature contour region slightly disagrees. Even though the crown thermocouples that are adjacent to the burner have a lower height ($z = 1.7$ m) than that in the front burner case ($z = 1.3$ m), the highest crown temperature of about 100 °C is similar to that in the front burner case. Finally, in the quasi-steady state and away from the burner, there is no obvious hindering impact from the ribs that lay along the path of the flow in either direction. A temperature increase is seen in the space between ribs on top of the burner (see Figure 17), indicating their local constraining effect.



(a) Temperature Slice at $y = 3.0$ m.



(b) Temperature Slice at $x = 2.3$ m.

Figure 17. Representative temperature slices at: (a) $y = 3$ m, (b) $x = 2.3$ m in Case 3. Time $t = 300$ s. Temperature units are in $^{\circ}\text{C}$

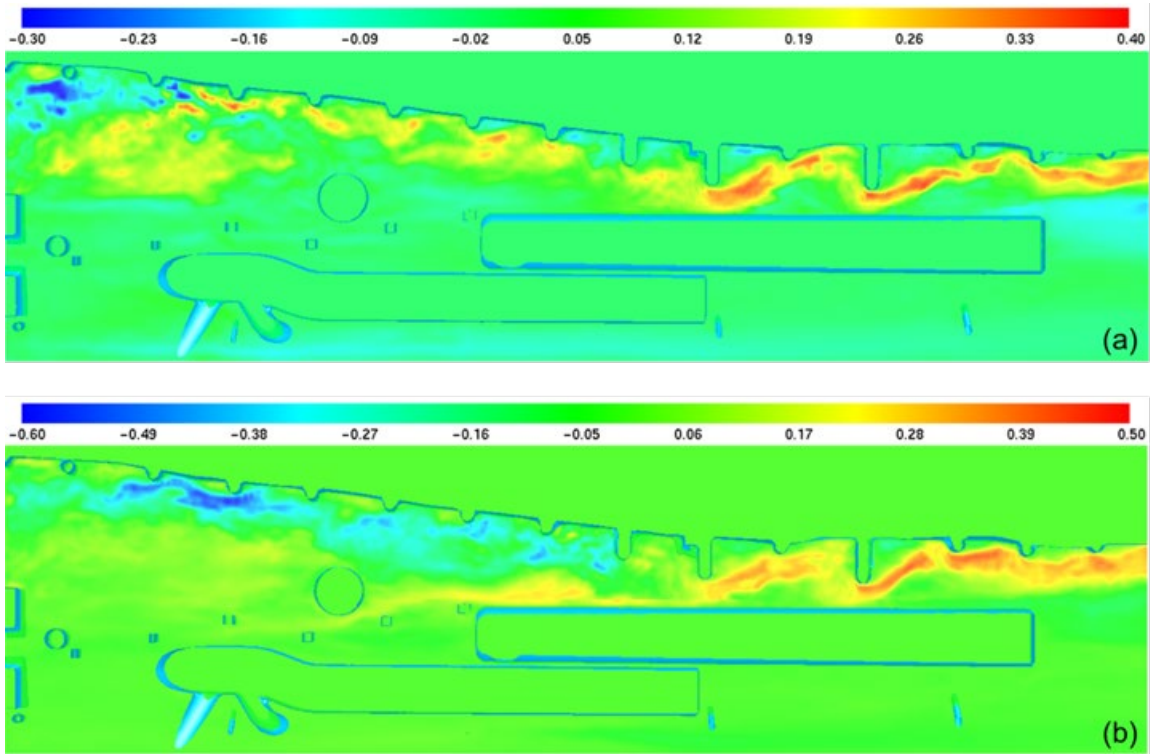


Figure 18. Comparison of velocity along x-axis at $y = 3$ m slice in: (a) Case 1, (b) Case 3. Time $t = 300$ s. Velocity units are in m/s

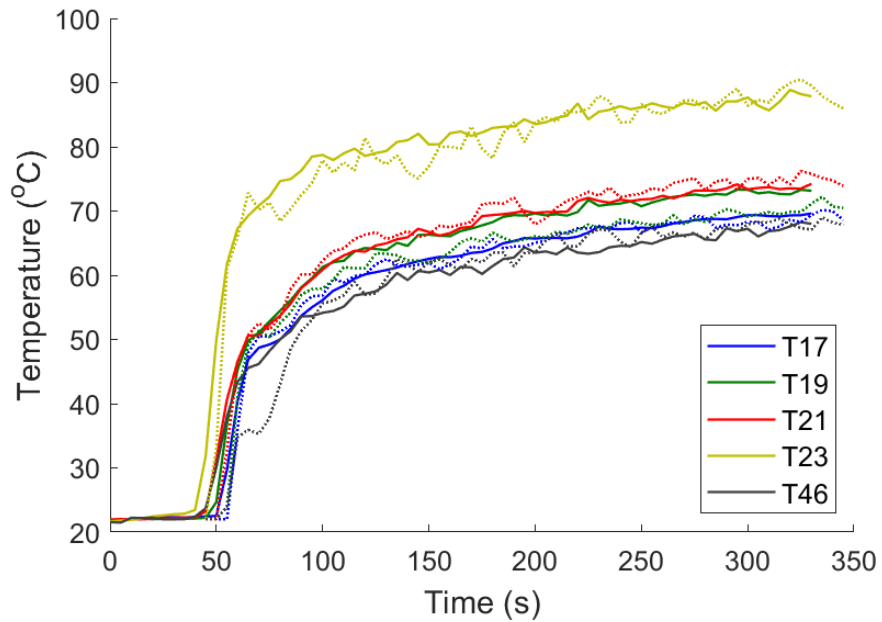


Figure 19. Measured (solid line) and modeled (dash line) temperature results of TCs at center along x direction (front – aft) in Case 3

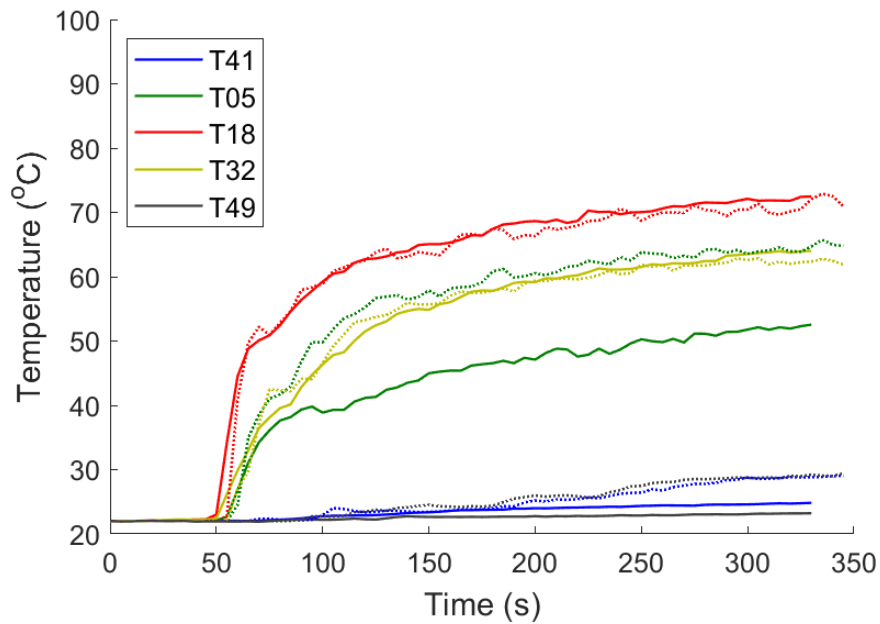


Figure 20. Measured (solid line) and modeled (dash line) temperature results of TCs near rear burner along y direction (side – side) in Case 3

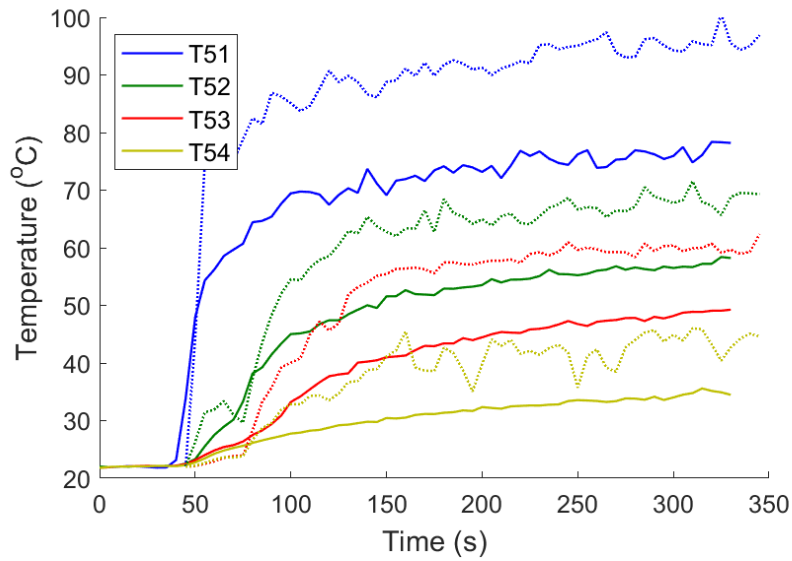


Figure 21. Measured (solid line) and modeled (dash line) temperature results of TCs at TC Tree A in Case 3

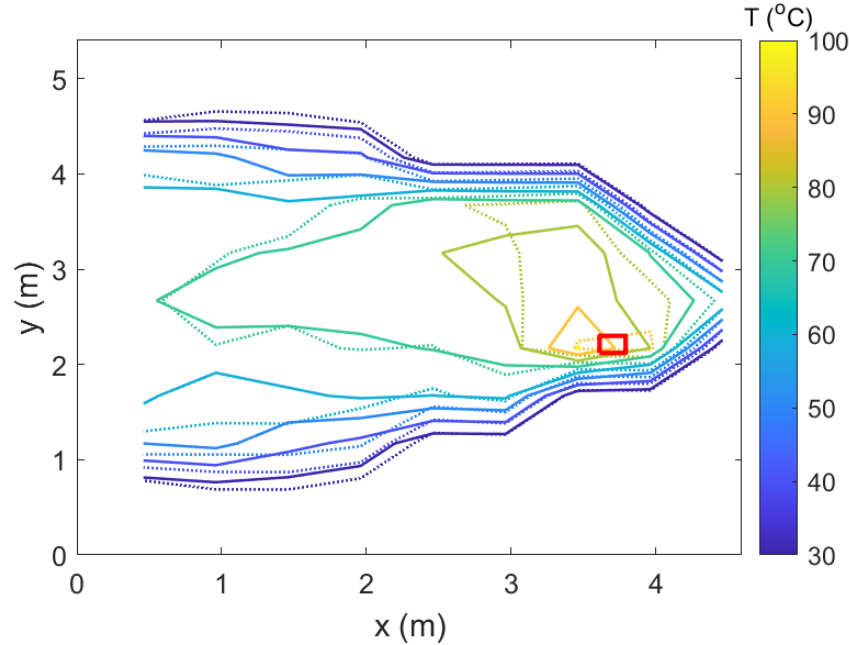


Figure 22. Contour map of measured (solid line) and modeled (dash line) temperature results of crown TCs in Case 3

5.4 Uncertainty analysis

The reproducibility among the 2-3 experimental replicates in three cases is calculated to be 1.5 °C. The standard limits of error provided by the K-type thermocouple manufacturer is less than 2.2 °C. The effect of the heat release rate uncertainty on temperature measurements (McGrattan, et al., Fire dynamics simulator, technical reference guide, September 2013) is estimated to be less than 0.5 °C. The temperature error from the uncertainty in thermocouple location is estimated to be 2.3 °C, based on the three-axis temperature gradient near thermocouple trees. Overall, the total uncertainty from thermocouple measurements is estimated to be 3.6 °C, which falls within the relative standard uncertainty of 5% recommended for validation data sets in Ref. (McGrattan, et al., Fire dynamics simulator, validation guide, September 2013).

For each crown and tree thermocouples, the temperature over the last 60 sec of sampling (indicating a quasi-steady state) is averaged. A model uncertainty analysis (McGrattan, et al., Fire dynamics simulator, validation guide, September 2013) is performed to compare the model predictions on each thermocouple with the measurements for the three cases, as indicated in Figure 23. Thermocouples with temperature increases over the duration of the experiment less than 5 °C are discarded from the analysis. Considering both crown and tree thermocouple readings, the model has a bias factor of 1.12, indicating over-prediction. The calculated relative standard deviation of the model, as defined in Ref. (McGrattan, et al., Fire dynamics simulator,

validation guide, September 2013), is 0.24. When using only crown thermocouples, the computed bias factor and relative standard deviation are 1.08 and 0.15 respectively. Note that ideally, in validation we seek to have the model error within the experimental uncertainty.

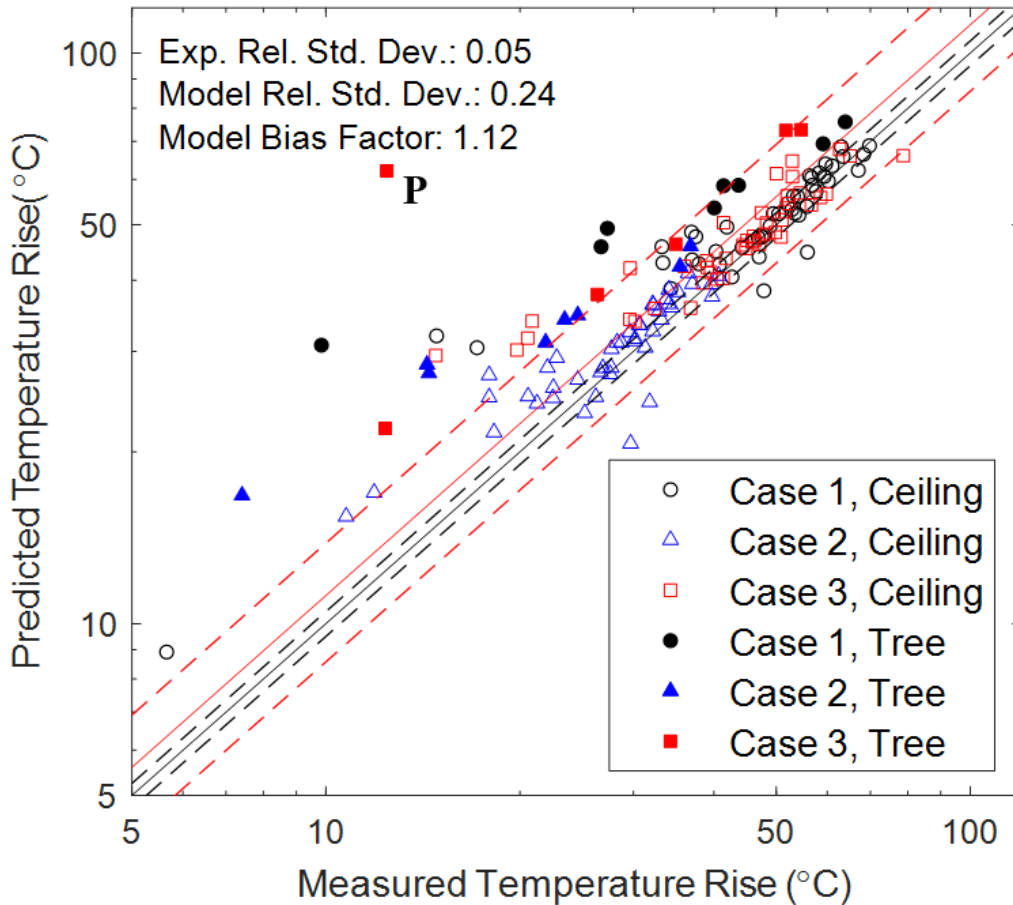


Figure 23. Measured vs. Predicted TC temperatures averaged over the last 60 s of experiment. The three experimental cases are shown. Filled symbols represent tree thermocouples, hollow symbols crown thermocouples. Point P is an outlier value for TC56 in the rear burner Case 3.

The model is intended to be used to predict fire detection at the earliest stage, where the onset time of temperature rise is important. The onset time of each thermocouple is defined as the time at which temperature reaches its half maximum above ambient temperature, $t_{\text{onset}} = (t_{T_{\text{max}}} - t_{T_{\text{amb}}}) / 2$. The modeled onset time of each thermocouple is compared with the experiments. Among thermocouples 17, 18, 19, 20, 21, 22, 23, 45, and 46 along the x-axis, the average modeled onset time is lower than the measured onset time by 5.6 s.

It is important to remark the higher differences between simulations and the thermocouple tree readings. For instance, the outlier point P in Figure 23 corresponds to TC56 (second from the

top) in thermocouple tree B for the rear burner experiment, Case 3. It is noted in Figure 24 that for the simulation this thermocouple lays within a hot zone with temperatures over 80 °C, while in the experiment it recorded a temperature of 35 °C. This demonstrates the challenge in replicating local variations of temperature between model and experiment. We speculate this is due to less mixing and a sharper boundary between cold and hot layers seen in simulations with respect to experiments. This is a known trait in compartment simulations, probably exacerbated here by the presence of small-scale clutter items (cables, rods, etc.) in the real compartment, not accounted for in computations.

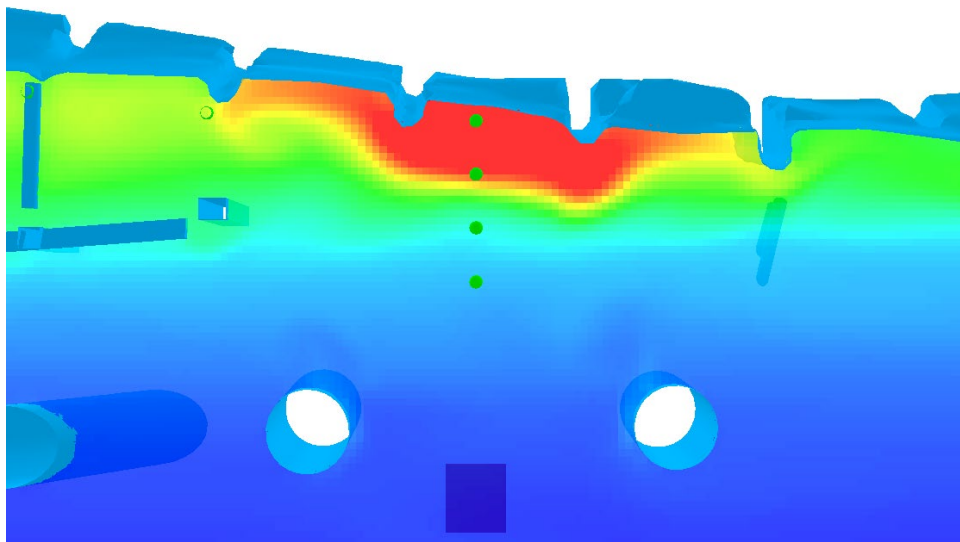


Figure 24. Average temperature contour along plane $Y = 1.73$ m (TC tree B) for Case 3. Temperatures from 22 °C (blue) to 85 °C (red) averaged over the last 60 sec. Thermocouples in green. The two higher thermocouples of Tree B (TC55, TC56) lay in a hot temperature region.

6 Summary

This study investigates the impact of a hidden fire in the overhead region of a large commercial aircraft. The experiments also serve as a validation for NIST’s development of a new unstructured geometry model. Full-scale fire tests within the overhead inaccessible-area for heat release rates of 5.5 kW and 11 kW and for two different fire source locations were performed. Thermocouple information at the curved crown level and within the region has been measured in these tests. In parallel, a set of simulations using an unstructured geometry model for overhead inaccessible-area in FDS using parameters specified for the tests were carried out.

A new FDS unstructured geometry simulation capability is currently under development. Model validation results are defined in terms of thermocouple readings measured and computed with

satisfactory overall agreement. The resulting hot spot due to the fire source is accurately identified using modeling. In general, timing of temperature onsets is also well captured, as well as the time dependency of temperature curves. In fire protection, the timeliness and location for detection are coupled and both need to be accurately predicted. In future practice, the model can potentially be used to identify hot areas where a sensitive item (e.g., battery box) is burning, and to predict the onset time to trigger alarms. The predicted crown temperatures are in the correct range, with 3 °C to 6 °C average and rms temperature differences among experiments and computations. It is found that the model and simulation setup used tends to over-predict temperatures with respect to tests as shown in section 5.4, also exhibiting a sharper transition region between cold and hot layers. In section 5.4, it is found that crown temperatures are slightly over-predicted, with modeled temperature increases biased with respect to experimental measurements by a factor of 1.08 and a relative standard deviation of 0.15.

In the front fire source location scenario, the hot layer height decreases while the hot gas gradually migrates towards the aft region. The crown temperature decreases with the decrease of the fire heat release rate in Case 2. For the aft fire source location, hot gas migrates to two directions: rising to the upper crown in front and flowing to the aft region, both help transport energy and avoid local hot spots. Flow in the front also recirculates back. Despite the fact that aft fire source is closer to the crown, the maximum temperature observed at its adjacent crown area, of about 100 °C, is similar to that in the front fire test. Review of gas temperature measurements for crown thermocouples TC16 and TC23 and the top Tree A thermocouple TC51 show that, for this case, rib thermocouples display higher temperatures than the TC51 reading. It is speculated that in the experiment the fire plume was tilted slightly forward as can also be inferred by looking at the crown temperature contour plot of Figure 22. Finally, it is noted that away from fire sources, the ribs that lay along the crown of the curved fuselage of the hidden space have only a minor hindering impact in the transport of hot gases and smoke. On the other hand, ribs located on top of the fire source impose a local constraining effect on the motion of hot gases.

7 References

- AFS-200. (December 2014). *Advisory Circular 120-80A, In-Flight fires*. Federal Aviation Administration.
- Balaras, E. (2004). Modeling complex boundaries using an external force field on fixed cartesian grids in large-eddy simulations. *Computers & Fluids*, 33, 375-404.
- Berger, M. (2017). Cut cells: meshes and solvers. In *Handbook of Numerical Analysis*.
- Conradi, K. (February 2015). *Report on the serious incident to Boeing B787-8, ET-AOP London Heathrow Airport on 12 July 2013*. Air Accidents Investigation Branch.
- Eymard, R., Gallouet, T., & Herbin, R. (2000). Finite volumes methods. In *Handbook of Numerical Analysis* (pp. 713-1020). Elsevier.
- Fadlun, E., Verzicco, R., Orlandi, P., & Mohd-Yusof, J. (2000). Combined immersed-boundary finite-difference methods for three-dimensional complex flow simulations. *Journal of Computational Physics*, 161, 35-60.
- Forney, G. (2020). *Smokeview, a Tool for Visualizing Fire Dynamics Simulation data vol. 1: Users Guide*. Gaithersburg, Maryland: National Institute of Standards and Technology.
- Gropp, W., Lusk, E., & Skjellum, A. (1999). *Using MPI - Portable parallel programming with the message-passing interface* (2nd Edition ed.). Cambridge, Massachusetts: MIT Press.
- Guo, H., Oztekin, E. S., Crowley, S., Scrofani, P., & Lyon, R. E. (February 2019). *Modeling of hidden fire in aircraft overhead area*. Federal Aviation Administration.
- Kirkpatrick, M., Armfield, S., & Kent, J. (2003). A representation of curved boundaries for the solution of the navier–stokes equations on a staggered three-dimensional cartesian grid. *Journal of Computational Physics*, 184, 1-36.
- LeVeque, R. (2002). *Finite volume methods for hyperbolic problems*. Cambridge University Press.
- McDermott, R. J. (2014). A velocity divergence constraint for large-eddy simulation of low-mach flows. *Journal of Computational Physics*, 274, 413-431.
- McDermott, R., & Vanella, M. (n.d.). *Evaluation of temperature wall functions for large-eddy simulation over curvilinear geometries*.

McGrattan, K., Hostikka, S., McDermott, R., Floyd, J., Weinschenk, C., & Overholt, K. (September 2013). *Fire dynamics simulator, technical reference guide*. Gaithersburg, Maryland, USA: National Institute of Standards and Technology.

McGrattan, K., Hostikka, S., McDermott, R., Floyd, J., Weinschenk, C., & Overholt, K. (September 2013). *Fire dynamics simulator, validation guide*. Gaithersburg, Maryland: National Institute of Standards and Technology.

Perot, J. (1993). An analysis of the fractional step method. *Journal of Computational Physics*, *108*, 51-58.